

# Ionic Colloidal Molding as a Biomimetic Scaffolding Strategy for Uniform Bone Tissue Regeneration

Jian Zhang, Jinpeng Jia, Jimin P. Kim, Hong Shen, Fei Yang,\* Qiang Zhang, Meng Xu, Wenzhi Bi, Xing Wang, Jian Yang, and Decheng Wu\*

Inspired by the highly ordered nanostructure of bone, nanodopant composite biomaterials are gaining special attention for their ability to guide bone tissue regeneration through structural and biological cues. However, bone malformation in orthopedic surgery is a lingering issue, partly due to the high surface energy of traditional nanoparticles contributing to aggregation and inhomogeneity. Recently, carboxyl-functionalized synthetic polymers have been shown to mimic the carboxyl-rich surface motifs of non-collagenous proteins in stabilizing hydroxyapatite and directing intrafibrillar mineralization in-vitro. Based on this biomimetic approach, it is herein demonstrated that carboxyl functionalization of poly(lactic-co-glycolic acid) can achieve great material homogeneity in nanocomposites. This ionic colloidal molding method stabilizes hydroxyapatite precursors to confer even nanodopant packing, improving therapeutic outcomes in bone repair by remarkably improving mechanical properties of nanocomposites and optimizing controlled drug release, resulting in better cell in-growth and osteogenic differentiation. Lastly, better controlled biomaterial degradation significantly improved osteointegration, translating to highly regular bone formation with minimal fibrous tissue and increased bone density in rabbit radial defect models. Ionic colloidal molding is a simple yet effective approach of achieving materials homogeneity and modulating crystal nucleation, serving as an excellent biomimetic scaffolding strategy to rebuild natural bone integrity.

To enhance mineralization, nanodopant composite polymers have been widely employed as bioactive scaffolds that can be loaded with synergistic nanoparticles (NPs) such as hydroxyapatite (HA), mimicking the complex inorganic–organic nanostructure of natural bone and significantly improving mechanical properties.<sup>[1–4]</sup> Despite the increased mineral content, however, most nanodopant composites poorly modulate crystal nucleation due to material inhomogeneity. Traditional methods of mechanical mixing or coprecipitation form slurries of aggregated NPs due to their high surface energies, resulting in sedimentation of these precursors and inhomogeneous distribution of NPs within the composite scaffold matrices.<sup>[5–7]</sup> Consequently, material inhomogeneity is a significant concern in orthopedic implants, with ramifications such as uneven HA loading, inefficient drug release, irregular cell in-growth, and uneven biomaterial degradation all contributing to poor modulation of biomineralization and irregular osseous repair, especially near regions of low fluid flow.<sup>[8–10]</sup> Several efforts to produce homo-

The limitations of autografts and allografts inherent to orthopedic surgery, including low supply and immunogenicity, have prompted the development of alternative biomaterials that can mimic the natural extracellular matrix and direct cell–material interactions that modulate biomineralization and osteointegration to promote uniform bone tissue regeneration.

geneous nanocomposites, including inorganic cement scaffolds and salt/polymer additives, still translate poorly in the repair of critical-size bone defects.<sup>[11–18]</sup> Very recent reports further reveal the lingering issues of bone malformation, e.g., incomplete bridging and irregular medullary cavities in autograft and medical-grade scaffolds,<sup>[19]</sup> uneven bone surfaces,<sup>[20,21]</sup> and

Dr. J. Zhang, Dr. H. Shen, Dr. F. Yang, Dr. X. Wang, Prof. D. Wu  
Beijing National Laboratory for Molecular Sciences  
State Key Laboratory of Polymer Physics and Chemistry  
Institute of Chemistry  
Chinese Academy of Sciences  
Zhongguancun North First Street 2, Beijing 100190, China  
E-mail: fyang@iccas.ac.cn; dcwu@iccas.ac.cn  
Dr. J. Zhang, Dr. F. Yang, Prof. D. Wu  
School of Chemistry and Chemical Engineering  
University of Chinese Academy of Sciences  
19 A Yuquan Rd, Shijingshan District, Beijing 100049, China

Dr. J. Jia, Dr. Q. Zhang, Dr. M. Xu, Dr. W. Bi  
Department of Orthopaedics  
General Hospital of Chinese People's Liberation Army  
28 Fuxing Road, Beijing 100853, China  
Dr. J. P. Kim, Prof. J. Yang  
Department of Biomedical Engineering  
Materials Research Institute  
The Huck Institutes of the Life Sciences  
The Pennsylvania State University  
University Park  
PA 16802, USA



DOI: 10.1002/adma.201605546

formation of multiple chambers.<sup>[22]</sup> Therefore, addressing bone malformation still remains a grand challenge for bone regeneration of critical-size defects by now.

Inspired by the central role of charged noncollagenous proteins (NCPs) in regulating intrafibrillar mineralization, recent works have employed ionic stabilization of nanodopants as a biomimetic strategy to modulate crystal nucleation. Specifically, NCPs such as osteocalcin and bone sialoproteins are rich in surface polycarboxylates from an abundance of aspartic acid and glutamic acid residues, acting as structural motifs that stabilize HA particles in solution but promote crystal nucleation once adsorbed onto a substrate, preventing aggregation of large HA crystals that typically lead to malformed or brittle bones.<sup>[23–25]</sup> A few studies have designed these synthetic polymers rich in carboxylate functional groups to improve biomineralization in vitro,<sup>[25]</sup> such as carboxylated dendrimers<sup>[26]</sup> and anionic polypeptides,<sup>[23]</sup> which, respectively, showed increased HA binding capacity and increased mineral loading on collagen scaffolds, whereas capping of carboxyl groups on bone sialoproteins destroyed its nucleation activity.<sup>[24]</sup>

However, despite the promising evidence in vitro, carboxyl-functionalized synthetic polymers have yet to be evaluated for bone regeneration in vivo, nor recognized as a mode of achieving material homogeneity. Hence in this work, we present ionic colloidal molding as a nanocomposite scaffolding strategy that employs carboxyl-modified poly(lactic-co-glycolic acid) (PLGA-COOH) to stabilize HA nanoparticles for bone tissue regeneration. This simple and highly processible molding method demonstrated great material homogeneity, with which we designed a nanocomposite scaffold that can serve as both a source of HA nanoparticles and a carboxyl-rich substrate to enhance biomineralization and modulate crystal nucleation. Our mechanical and in vitro studies revealed that even nanodopant packing within carboxyl-functionalized PLGA substrates enhanced osteogenesis and biomineralization compared with traditional PLGA–HA<sup>[14–16]</sup> substrates. More notably, our 60 and 150 d in vivo studies on critical-sized rabbit radial defect models demonstrated that scaffolds prepared by ionic colloidal molding significantly improved osteointegration and reduced chronic inflammation, likely due to better controlled biomaterial degradation, producing highly regular bone tissue resembling intact bone. Taken together, ionic colloidal molding is a simple, biomimetic approach of achieving material homogeneity and modulating crystal nucleation to promote uniform bone tissue regeneration.

To achieve even dispersion of HA-NPs within PLGA complexes, we modified the terminal hydroxyl groups of PLGA with carboxyl end groups using succinic anhydride to form PLGA-COOH (Figure 1a and Figure S1 (Supporting Information)). HA-NPs were prepared by emulsion via mixing calcium acetate hydrate with potassium phosphate tribasic monohydrate, followed by calcination under 800 °C (Figure S2, Supporting Information)<sup>[27]</sup> Excitingly, this simple modification step demonstrated profound effects on nanoparticle stability, as HA-NPs dispersed in PLGA-COOH solution maintained homogeneity even after 5 h, compared to rapid precipitation ( $\approx 10$  s) in dioxane and slow precipitation ( $\approx 1$  h) in PLGA (Figure 1b and Figures S3 and S4 (Supporting Information)). These observations were supported by transmission electron microscopy

(TEM) which revealed that HA-NP/PLGA-COOH complexes dispersed well into hundreds of nanoclusters, while HA-NPs alone aggregated into dense microparticles and HA-NP/PLGA complexes assembled into loose microparticles (Figure 1c and Figure S5 (Supporting Information)).

The observed increase in dispersion stability from pure HA-NP to HA-NP/PLGA, then to HA-NP/PLGA-COOH can be explained in terms of the molecular surface interactions involved (Figure 1d,e). HA-NPs tend to form large aggregates due to the high ionic surface attractions stemming from extensive distribution of  $\text{Ca}^{2+}$ ,  $\text{PO}_4^{3-}$ , and  $\text{OH}^-$  ions on the surface.<sup>[12]</sup> Even with the addition of PLGA, as in traditional composite methods of coating nanoparticles, the hydroxyl end groups only provide weak repulsion among the adsorbed HA-NPs, forming loose aggregates (Figure 1c–e). Finally, our molding strategy is based on achieving ionic colloidal dispersion of nanoparticles, as the introduction of the carboxyl group to PLGA provides strong repulsion against the  $\text{Ca}^{2+}$  ions in HA-NPs, forming stable colloids with HA-NP core/PLGA shell structures (Figure 1d). As support, TEM shows peripheral polymeric layers of HA-NPs after 24 h mixing in PLGA-COOH solution (Figure 1c).

To better understand the design principles behind stable core/shell nanocolloids, we reproduced ionic colloidal dispersion with other nanoparticles. Similar to HA-NPs,  $\text{CaCO}_3$  and tricalcium phosphate (TCP) nanoparticles exhibited superior dispersion in PLGA-COOH compared to PLGA and dioxane (Figure S6, Supporting Information). However, neutral  $\text{SiO}_2$  showed no improvement in dispersion stability or assembled morphology in PLGA-COOH compared to PLGA, demonstrating that strong electrostatic interaction between NPs and polymers is essential to yield stable core/shell nanocolloids (Figure S7, Supporting Information).

Next, we applied ionic colloidal dispersion as a molding method to fabricate nanocomposite scaffolds<sup>[28,29]</sup> to study how dispersion stability affects mechanical and material properties. The nanocomposite scaffold constructed from ionic colloidal precursors of HA-NP/PLGA-COOH (termed “Ion-scaffold”) was compared to scaffold constructed from mixed dispersion of HA-NP/PLGA (termed “Mix-scaffold”) as control, both prepared from an established solvent casting and particle leaching method.

To compare NP uniformity within the scaffolds, we anchored HA-NPs with Evans Blue, which showed dense colors accumulated near the bottom of the Mix-scaffold, indicating deposition of HA-NPs, whereas the blue color was homogeneously distributed throughout the Ion-scaffold, indicating uniform NP distribution (Figure 2e,g). These observations were confirmed by scanning electron microscope (SEM), in which Mix-scaffold morphology revealed rough, aggregated micrometer-sized particles, resulting in structural defects such as fissures and cracks (Figure 2f and Figure S10 (Supporting Information)). In contrast, the Ion-scaffold morphology showed even encapsulation of HA-NPs within the PLGA matrix (Figure 2h and Figure S10 (Supporting Information)). The observed differences were quantified by thermogravimetric analysis (TGA) to determine inorganic HA-NP content at the top, middle, and bottom layers of the 20 mm scaffolds (at 19, 10, and 1 mm heights, respectively) after burning away the organic PLGA components.

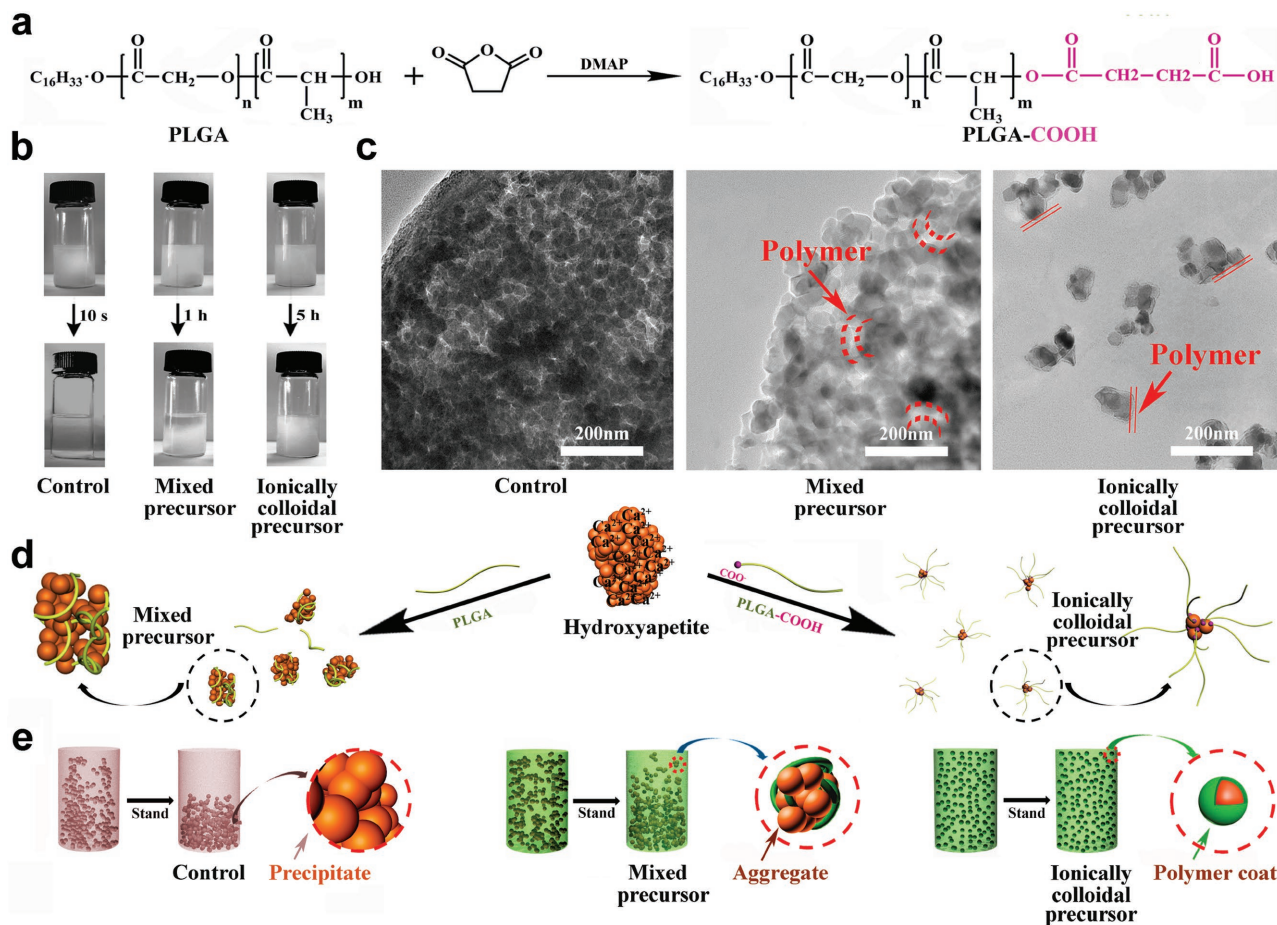


**Figure 1.** Formation of stable PLGA-COOH/nanohydroxyapatite (HA-NPs) colloid. a) The PLGA-COOH was synthesized via modification of end hydroxyl groups of PLGA into carboxyls. b) Stability evaluation of the pure HA-NPs (control), PLGA/HA-NPs (mixed precursor), and PLGA-COOH/HA-NPs (ionically colloidal precursor) in dioxane, showing that HA-NPs quickly precipitated on its own, slowly precipitated in PLGA solution, and dispersed well in the PLGA-COOH solution. c) Representative TEM images of the HA-NPs (control), PLGA/HA-NPs (mixed precursor), and PLGA-COOH/HA-NPs (ionically colloidal precursor) in dioxane, showing that pure HA-NPs aggregated into dense microsized particles, PLGA absorbed HA-NPs to aggregate into loose microsized particles, while PLGA-COOH coated HA-NPs formed nanosized particles. d) PLGA-COOH is proposed to form a stable ionically colloidal precursor that can efficiently bind, disperse, and stabilize HA-NPs at the nanoscale level via electrostatic interactions. e) Illustration of stability discrepancy among the above three groups.

As expected, the Ion-scaffold showed homogeneous dispersion of HA-NPs throughout the three layers, at  $\approx 50\%$  HA-NP content in agreement with its 1:1 feed ratio (Figure 2j), while the Mix-scaffold had HA-NP contents of 46%, 50%, and 56% in the top, middle, and bottom layers, respectively (Figure 2i). As further support, we prepared films from mixed dispersion (termed “Mix-film”) and ionic colloidal precursors (termed “Ion-film”) to better characterize surface properties. The discrepancy in surface properties between the two films were clearly distinguishable by eye and SEM, with the Mix-film showing much larger aggregates and rougher surfaces compared to the Ion-film (Figure 2a–d).

The association between uniformity in composite materials and structural stability is well documented, as irregularity can lead to inert problems such as microcracks, stress-induced fractures, defect structure, secondary crack and even low stress breakage, substantially diminishing mechanical properties. Thus we studied how nanoparticle uniformity would affect mechanical properties

of nanocomposites by measuring the longitudinal compression modulus of the Ion-scaffold, Mix-scaffold, and polymeric control scaffolds (pure PLGA or PLGA-COOH) without HA-NP. Stress-strain curves showed that the compression modulus of the Mix-scaffold was  $\approx 2.06$  MPa, compared to 1.46 MPa of the pure PLGA scaffold (lacking HA-NP), indicating that the addition of HA-NPs to PLGA rendered only nominal mechanical improvements (Figure 2l). On the other hand, the compression modulus of the Ion-scaffold was 4.06 MPa, twice higher than that of the pure PLGA-COOH scaffold (1.89 MPa), indicating that particle uniformity is essential to fully realizing the nanometer toughening effect for mechanical enhancement (Figure 2l). The Ion-scaffold maintained superior compression modulus (1.43 MPa) even after fully swelling in phosphate-buffered saline (PBS) buffer for two months compared to the Mix-scaffold (0.96 MPa), PLGA-COOH scaffold (0.91 MPa), and PLGA scaffold (0.82 MPa) (Figure S11, Supporting Information). Similar longitudinal mechanical tension results were obtained with

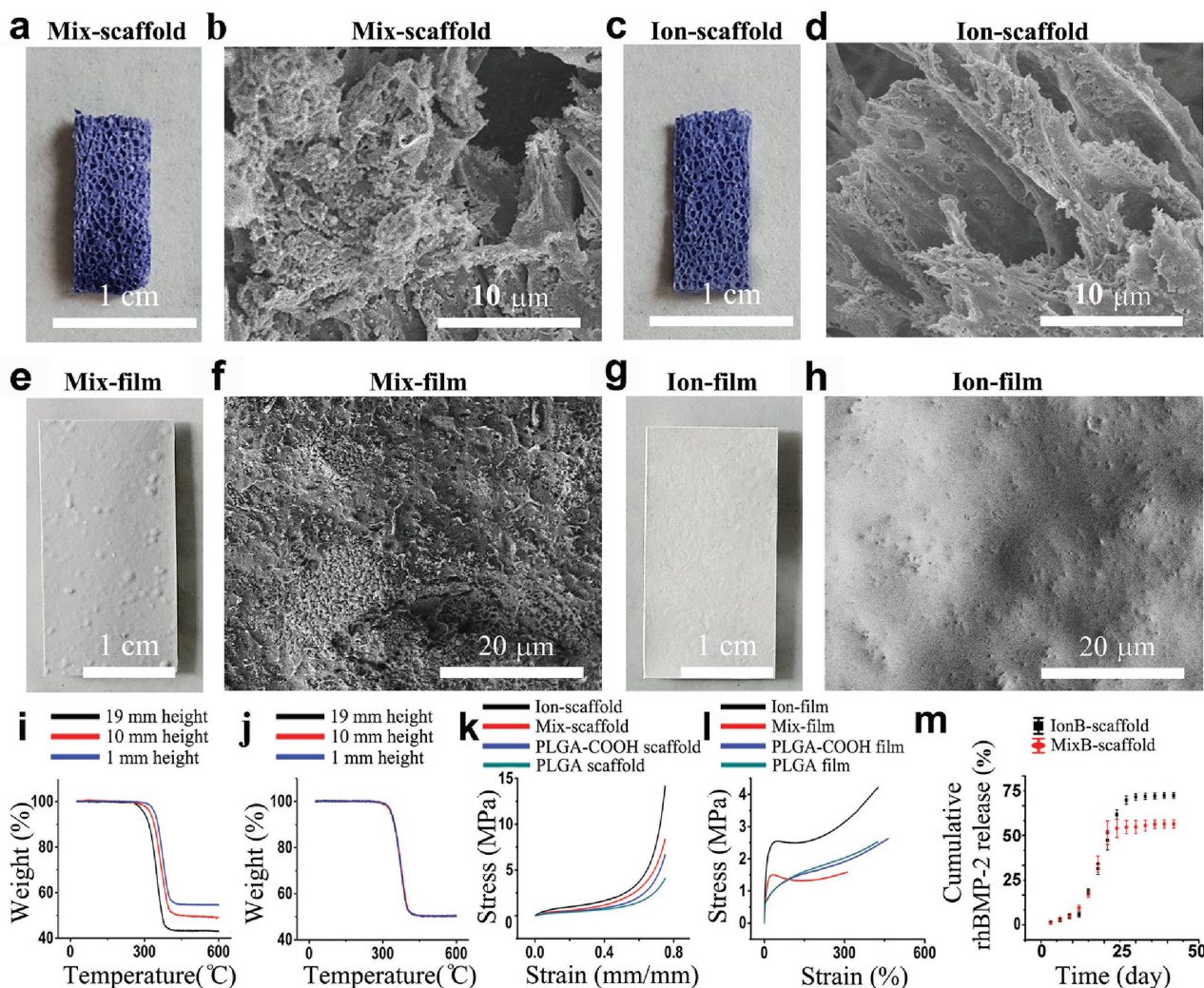


**Figure 2.** Comparison of various biomaterials fabricated from the mixed precursor (i.e., Mix-film or Mix-scaffold) and ionically colloidal precursor (i.e., Ion-film or Ion-scaffold). a–h) Representative digital photos (a,c,e,g) and SEM images (b,d,f,h) of PLGA/HA-NPs “Mix-film,” (a,b), PLGA-COOH/HA-NPs “Ion-film,” (c,d), PLGA/HA-NPs “Mix-scaffold,” (e,f), and PLGA-COOH/HA-NPs “Ion-scaffold” (g,h). i,j) Thermogravimetric analysis (TGA) of top, middle, and bottom slices of various scaffolds revealed bottom-heavy distribution of HA-NPs in the Mix-scaffold (i) and uniform dispersal of HA-NPs in the Ion-scaffold (j). k) Representative stress–strain curves obtained with uniaxial elongation measurements of the elastic modulus of Ion-film, Mix-film, and pure polymeric films. l) Representative stress–strain curves obtained with uniaxial compression examination of the Ion-scaffold and Mix-scaffold. m) The growth factor rhBMP-2 was encapsulated into the Mix-scaffold and Ion-scaffold to measure release profiles of the loaded scaffolds (respectively, referred to as MixB-scaffold and IonB-scaffold),  $N = 3$ .

the corresponding films, with superior tensile strength (elastic modulus) for the Ion-film (7.16 MPa) compared to the Mix-film (4.28 MPa), PLGA film (1.29 MPa), and PLGA-COOH film (1.29 MPa) (Figure 2k). Interestingly, the Ion-film performed just as well as pure polymeric films at maintaining elongation at break, although the Mix-film suffered from reduced elongation ratio due to defects within its structures.

We next evaluated the drug loading capacity of our scaffolds by introducing rhBMP-2, one of the most potent growth factors used in osteogenesis, into our molding method. HA-NPs physically anchored with rhBMP-2 were incorporated into the fabrication process (loading 3 μg per 0.25 g HA-NP), with the resultant scaffolds termed “MixB” using the mechanically mixed dispersion or “IonB” using the ionic colloidal dispersion. We washed surface-absorbed NPs from each scaffold during

the removal of porogen to avoid an initial burst release. The IonB scaffold possessed higher drug loading capacity (72%) over the MixB scaffold (56%) according to their release profiles (Figure 2m). We speculate that the uniform PLGA-COOH coating of HA-NPs, supported by SEM images (Figure 1c), provided effective shielding to yield higher drug loading capacity.

Following, we studied the role of nanocomposite uniformity on cellular attachment, proliferation, and osteogenesis through in vitro evaluation of our biomaterials. Slices (1 mm thick) were cut crosswise at the 19, 10, and 1 mm heights of the Mix-scaffold and Ion-scaffold to obtain “Mix1–3” and “Ion1–3”, respectively, where Mix1 refers to the slice obtained from the Mix-scaffold at 19 mm height, with four slices per study or time point. Each slice was cultured for osteogenic differentiation using MC3T3-E1, a mouse calvaria-derived osteoblastic cell line, to evaluate

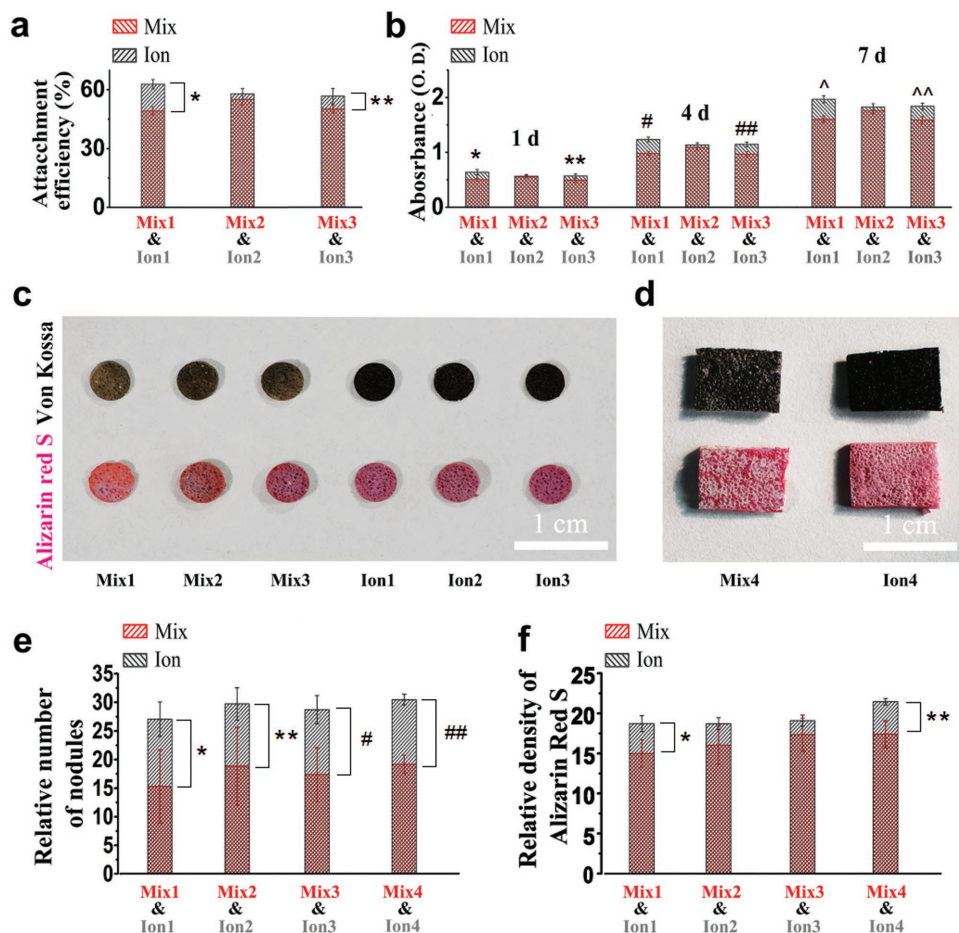


**Figure 3.** Evaluation of cell attachment, proliferation, and differentiation in vitro. a) Cell attachment efficiency and b) proliferation were evaluated in three “Mix” and three “Ion” scaffolds (labeled numerically Mix1–3 and Ion1–3) by horizontal slices of the cultured scaffolds at 1, 10, and 19 mm heights. Statistically significant improvements were observed with the Ion scaffolds at the 1 and 19 mm heights for all studies and time points ( $N = 4$ ,  $p < 0.05$ ). c,d) Von Kossa and Alizarin Red S staining of horizontal slices with osteogenic differentiation in vitro for 21 d. Mix1–3 and Ion1–3 were cut crosswise from 19, 10, and 1 mm height of the Mix-scaffold and Ion-scaffold, respectively. Significant improvements were observed in Ion scaffolds across all slices ( $N = 4$ ,  $p < 0.05$  for \*, \*\*, #, ##, ^, ^^). Mix4 and Ion4 were cut lengthwise from the Mix-scaffold and Ion-scaffold, respectively. e,f) The calcified nodules number and Alizarin Red S intensity of Mix1–4 and Ion1–4, showing significant improvements in Ion scaffolds in the 1 mm layer and columnar slices ( $N = 4$ ,  $p < 0.05$  for \*, \*\*, #, ##).

osteogenic performance of scaffold slices at the chosen z-positions. Moreover, the Mix-scaffold and Ion-scaffold were also cut lengthwise to obtain semicircular columns labeled “Mix4” and “Ion4” to track osteogenic performance along the scaffold z-axis. The Ion-scaffold performed better in cell attachment efficiency and cell proliferation at all three layers than those of the Mix-scaffold and with higher consistency. While 62%, 58%, and 57% of cells attached to the Ion1–3, respectively (a range of 5%), 45%, 55%, and 50% of cells attached to the Mix1–3, respectively (a range of 10%), indicating enhanced, uniform cell entrapment in the Ion-scaffold (Figure 3a). Statistically significant improvements were noted for the Ion-scaffold groups at the 1 and 19 mm slices ( $p < 0.05$ ). Next, viability of each scaffold layer was assessed with 1, 4, and 7 d proliferation assays, showing similarly enhanced proliferation in the Ion-scaffold layers compared to those of the Mix-scaffold (Figure 3b). These results demonstrated that uniform dispersion of HA-NPs

enabled better cell penetration and enhanced interfacial cellular adhesion to scaffolds.

Next, the osteogenic performance of each scaffold layer was evaluated with Von Kossa<sup>[30]</sup> and Alizarin red S<sup>[31]</sup> stains to measure mineralization markers such as alkaline phosphatase and calcium. In line with the previous results, Ion1–3 layers yielded darker colors and even color distribution after a 21 d culture compared to the Mix1–3 layers, with similar trends in the relative number of calcified nodules and relative intensity of Alizarin Red S staining, indicating superior osteogenic performance (Figure 3c,e,f and Figure S12 (Supporting Information)). Similar results were also obtained from the columnar slices of Ion4 and Mix4 cut lengthwise (Figure 3d,e,f). We speculate that carboxyl-functionalized PLGA may have also contributed to the increase in mineralization through enhanced HA binding capacity, as shown for carboxylated dendrimers,<sup>[32]</sup> though the extent of contribution will require further investigation.

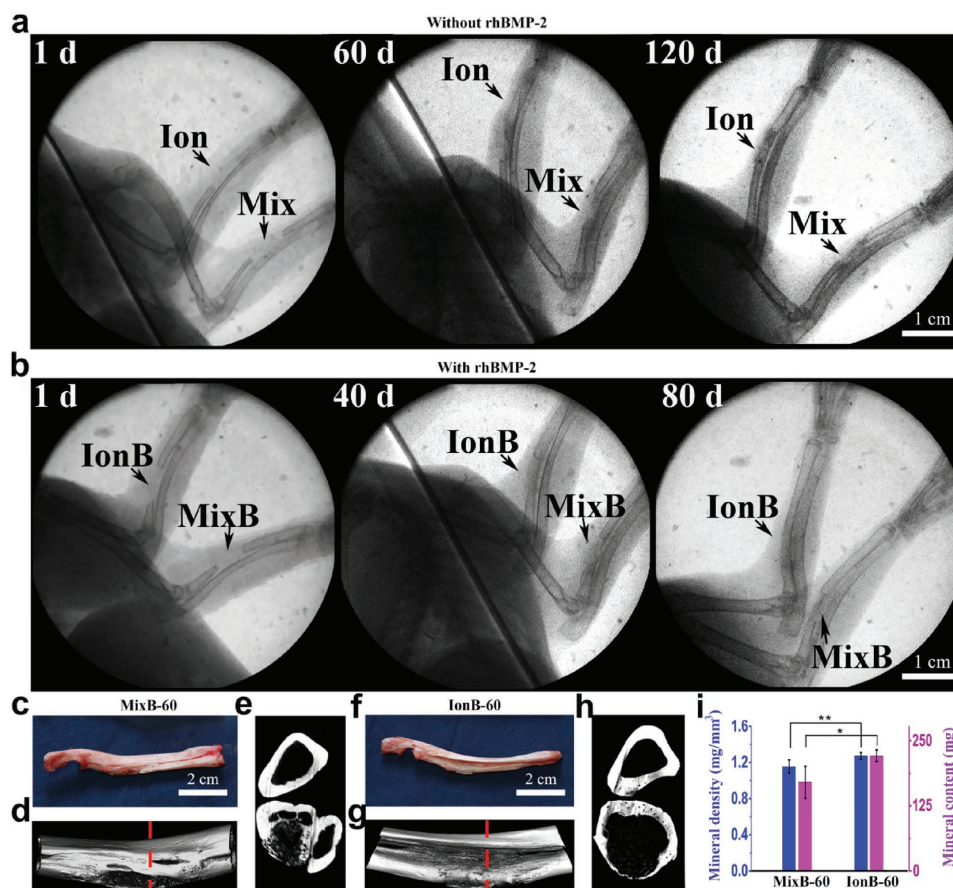


**Figure 4.** In vivo assessment of osteogenic performance. a,b) Representative X-ray images of 2 cm defects in rabbit radius demonstrated that the Ion-scaffold had superior osteogenic performance over the Mix-scaffold (a), with similar differences in improvement upon loading rhBMP-2 onto both scaffolds (b). The various scaffolds used in defect repair are labeled with an arrow along with abbreviated names Ion, Mix, IonB, and MixB. c–h) Assessment of bone tissue regeneration upon implantation of MixB-scaffold (MixB-60) and IonB-scaffold (IonB-60) for 60 d. Digital photos (c,f) and micro-CT images (d,e,g,h) of the new bones, while cross-sectional views (e,h) are selected from the dotted red lines (d,e), respectively. i) Comparison of mineral density and mineral content of MixB-60 and IonB-60, showing statistically significant improvement of the IonB-60 group in both studies ( $N = 3$ ,  $p < 0.05$  for \*, \*\*).

The above in vitro results were further supported by in vivo studies of bone regeneration using critical-size radial defect models in New Zealand rabbits. To evaluate long-term bone repair, we chose the 20 mm defect, widely considered a standard critical size even for larger animals, such as sheep<sup>[19]</sup> and monkeys,<sup>[20]</sup> as complete repair (including recanalization of the medullary cavity) takes around half a year even with scaffold implantation. Six study groups were implemented, with eight rabbit shoulders per group, by implanting the Mix-scaffold, Ion-scaffold, MixB-scaffold, IonB-scaffold, negative control (defect with no implantation), and positive control (intact radius) into the left or right radial defect of rabbits (see Section S9.1 in the Supporting Information for additional details). X-ray radiography was used to assess regenerated bone morphology in situ, which showed formation of new bone around the Ion composites in as early as 60 d, marked by a callus bridging the distal ends of the radial defect, even though the Mix group showed no complete regeneration even after 120 d (Figure 4a). With the addition of rhBMP-2, the IonB groups achieved near complete healing in as little as 40 d according to X-ray radiography. On the other hand, the MixB group even after 80 d showed poor

bone remodeling around the calcified bone interface and native bone margins, suggesting slow healing and malformed trabecular bridging (Figure 4b).

For postimplantation follow up, we removed the radial bone from three Mix-B and Ion-B scaffold groups after 60 d (three rabbits per study group). Reconstructed images from micro-computed tomography (Micro-CT) showed good osteointegration and new bone formation in contact with implants for both scaffold groups (Figure 4c,d). However, the MixB-60 group showed large, aggregated scaffold remnants, with regenerated bone forming multiple chambers with irregular medullary cavities, indicating bone malformation that is commonly seen with many traditional bone scaffolds (Figure 4e). Remarkably, regenerated bone from the IonB-60 group showed much smoother rebridging along the critical-size defect, controlled osteointegration of new bone tissue, and better dispersal of smaller scaffold remnants that are visible inside the medullary cavity (Figure 4g,h). Mineral volume, density, and content in regenerated bone were also significantly higher in the IonB-60 group ( $p < 0.05$ ), confirming that the ionic colloidal method indeed produced stronger bones (Figure 4i).

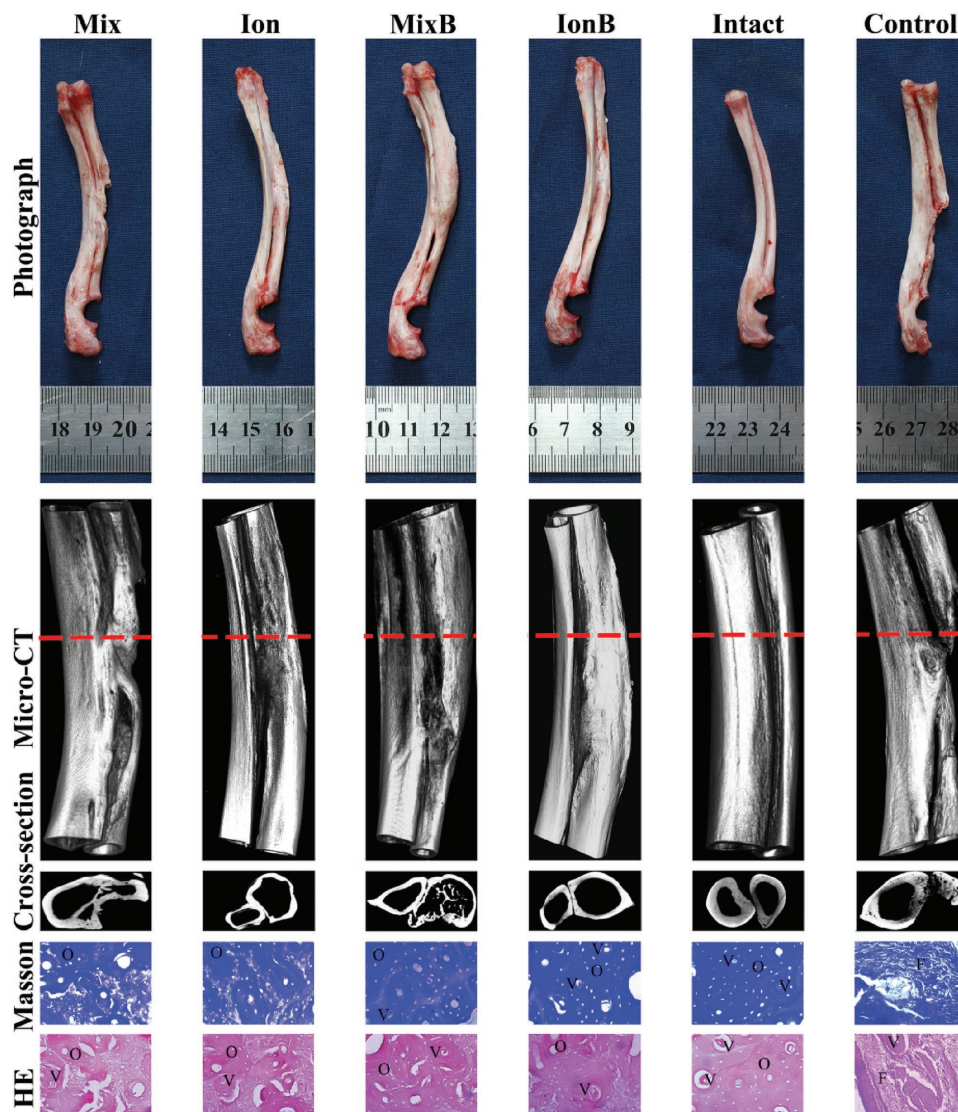


**Figure 5.** Evaluation of bone repair in critical sized rabbit radial defect models after 150 d postimplantation, with representative images of each study group labeled “Mix,” “Ion,” “MixB,” and “IonB” to refer to respective scaffolds implanted onto the radius defect, while “Intact” refers to the no-defect radius and “Control” refers to the self-repair of the radius defect without implants. Ion and IonB scaffolds showed better bone regeneration and formation of regular bone chambers on par with intact bone. The cross-sectional views of the new bones are, respectively, selected from the dotted red lines right above. In histological evaluation of H&E staining and Masson staining, F refers to fibrous tissue, O refers to osteocyte, and V refers to vessel.

To measure long-term therapeutic outcomes, we removed the radial bone from all the scaffold groups of the remaining rabbits after 150 d to allow full maturation of bone and complete degradation of biomaterials. Complete scaffold degradation is supported by H&E (Hematoxylin and Eosin) and Masson staining, while full bone maturation is supported by the presence of embedded osteons and vessels in the central canals (Figure 5). The same bone malformation with multiple bone chambers is seen with the Mix and MixB-scaffolds in Micro-CT, while regenerated bone from the Ion and IonB-scaffolds is similar to intact (no defect) bone (Figure 5). H&E staining showed that the IonB-scaffold elicited significantly less fibrous tissue encapsulation compared to the other scaffolds, indicating much better modulation of the chronic inflammatory response (Figure 5). To compare bone density and hardness,

we performed nanoscratch testing and bone mineral density measurement with dual-energy X-ray absorptiometry. While differences between the MixB and IonB groups in bone mineral density were not statistically significant ( $p > 0.05$ ), the Ion group showed significant improvement over the Mix group ( $p < 0.05$ ) (Figure 6c). Bone hardness tests did not reveal any significant improvements (Figure 6b). Moreover, the nanoscratch testing profiles reveal that the Ion and IonB-scaffolds yielded stronger and more uniform surface hardness compared to that of the Mix and MixB-scaffolds (Figure 6a). The density of regenerated bone in the Ion and IonB groups were 0.31 and 0.33  $\text{g cm}^{-2}$ , higher than that of the Mix (0.25  $\text{g cm}^{-2}$ ) and MixB (0.28  $\text{g cm}^{-2}$ ) groups, and even of intact bone (0.30  $\text{g cm}^{-2}$ ) (Figure 6b and Figure S15 (Supporting Information)). The above data suggest that bone regeneration performed with Ion

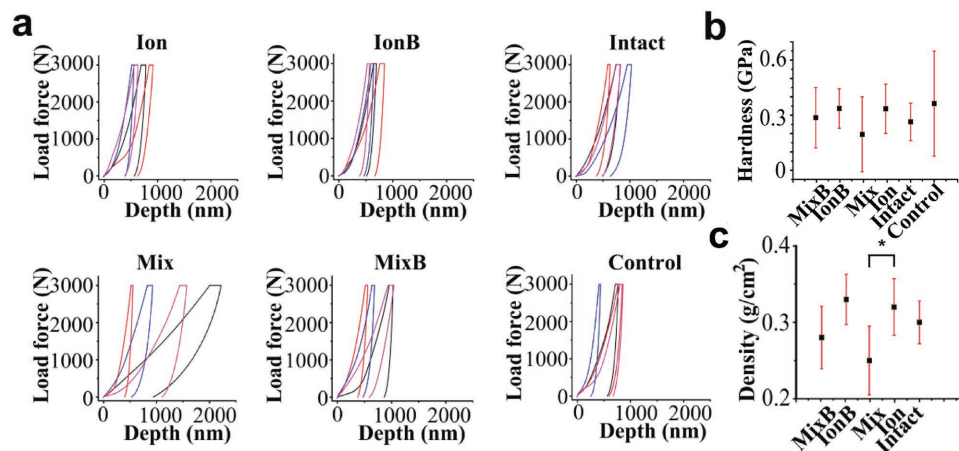


**Figure 6.** Mechanical hardness and strength of regenerated bones from various scaffolds after 150 d postimplantation. a) Nanoscratch testing profiles of representative radial bones in each study group. Four random points on the surface of each new bone were selected for testing. b) Hardness of regenerated bones. c) Bone mineral density of the regenerated bones ( $N = 5$ ,  $p < 0.05$  for \*).

and IonB-biomaterials yielded much stronger bones. We speculate that the formation of multiple chambers and irregularity of regenerated bone from traditional molding methods led to unnecessary bone volume and lower bone density, yielding brittle bones in the Mix and MixB groups. In contrast, uniform degradation of the Ion and IonB scaffolds due to even nanodopant packing may have better modulated osteointegration, whereas the Mix and MixB scaffolds cracked into large, irregular remnants. As fluid exchange is relatively low near the radial bone, the quality of biodegradation can significantly influence biodistribution of calcium and growth factors, hence guiding osteointegration and chronic inflammation. Further, as carboxyl-functionalized synthetic polymers were shown to mimic NCPs in coordinating HA nanoparticles and regulating intrafibrillar mineralization,<sup>[23]</sup> we hypothesize that solubilized PLGA-COOH during scaffold degradation may have contributed as an active polyanionic compound in favor of natural osteointegration, inhibiting large crystal nucleation to induce highly regular bone tissue regeneration. Further work will be needed to investigate the role of free PLGA-COOH in intrafibrillar mineralization.

In this work, we describe the development of uniform nanocomposite films and scaffolds based on our new ionic colloidal molding method, in which steady self-assembled liquid precursors are combined with carboxyl-functionalized biodegradable polymers and hydroxyapatite nanoparticles dispersed in organic solvents. Our studies suggest the following progression in favor of uniform bone tissue regeneration: (1) ionic colloidal molding stabilizes HA precursors to confer even nanodopant packing, remarkably improving mechanical properties, drug loading efficiency, and controlled drug release, contributing to (2) spatially regular cell penetration and in-growth to optimize signaling cascades for osteogenic differentiation. (3) Carboxyl-functionalized PLGA substrates may also enhance HA binding capacity, contributing to the observed *in vitro* increase in mineral deposition. (4) Material homogeneity enables better controlled biomaterial degradation, improving osteointegration and reducing chronic inflammation, translating to highly regular bone formation with structural and mechanical properties on

par with that of intact bone according to our *in vivo* studies on rabbit radial defect models. These exciting *in vitro* and *in vivo* results suggest that simple carboxyl-functionalization alone exerts considerable influence over the osteoinductive properties of nanocomposites and may lead to new generations of orthopedic biomaterials that properly address material surface interfaces that regulate cellular functions.

## Experimental Section

**PLGA and PLGA-COOH Preparation:** PLGA (with a molar ratio of lactide unit and glycolide unit about 1:1, molecular weight about 85 000) was prepared by ring-opening polymerization of L-lactide and glycolide with molar ratio 1:1 in sealed glass ampoules at 180 °C for 20 h in the presence of stannous octoate. The raw PLGA was purified by dissolving in chloroform and reprecipitation from ethanol and then followed by drying in vacuum. The carboxylate modified PLGA (PLGA-COOH) was prepared by dissolving PLGA, succinic anhydride, and 4-(dimethylamino) pyridine (DMAP) in dichloromethane. The mixture was stirred for 4 h at room temperature before it was concentrated. The PLGA-COOH was achieved by precipitation from methanol and then followed by drying under vacuum.

**HA-NP Preparation:** HA-NPs with average diameters about 45 nm were produced. Briefly, based on the theory of critical micelle concentration, hexadecyl trimethyl ammonium bromide (CTAB) was used to regulate the size of HA-NPs. Calcium acetate hydrate solution and potassium phosphate tribasic monohydrate solution with the same molarity (0.15 M) were blended in the presence of CTAB. The product was isolated with centrifugation and washed using citric acid solution whose pH was adjusted with ammonium hydroxide to about 9. The centrifugally separated slurries were washed, lyophilized, and then calcinated.

**Films and Scaffold Preparation:** For mechanical properties' comparison, films and scaffolds were prepared with a common method. In short, to prepare the films, an ionic colloidal precursor of PLGA-COOH, HA-NPs, and dioxane with a weight ratio 1:1:6 (or a mixed precursor of PLGA, HA-NPs, and dioxane with the same weight ratio) were cast onto polytetrafluoroethylene (PTFE) plates after 24 h stirring. After being air dried at room temperature for 24 h, the obtained PLGA-COOH/HA-NPs films (or PLGA/HA-NPs films) were removed from the plates and further vacuum dried thoroughly. For control experiment, PLGA-COOH films (and PLGA films) were prepared as follows: a PLGA-COOH/dioxane solution with a weight ratio 1:3 (or a PLGA/dioxane solution with the same weight ratio) was cast onto PTFE plates then dried by the same

processes. The thickness of all the films was about 0.5 mm. To prepare the scaffolds, after 24 h of stirring, the PLGA-COOH/HA-NPs/dioxane ionic colloidal precursor (or PLGA/HA-NPs/dioxane mixed precursor) with the same weight ratio as describe above was stirred with preserved NaCl particles (with average diameters about 250  $\mu\text{m}$ , weight ratio to dioxane 1:1, used here as porogen) and then cast into PTFE cylinder molds (two size molds were used: 5 mm diameter  $\times$  20 mm high and 8 mm diameter  $\times$  12 mm high). After being frozen and subsequently lyophilizing to remove any remaining solvent, the resulting polymer/salt composites were then immersed in distilled water to leach out the salt. The fabricated scaffold was dried and kept in a desiccator. The porosity of all these foams was about 90%  $\pm$  2% as determined according to literature.<sup>[33]</sup> PLGA-COOH and PLGA scaffolds were also fabricated by the same processes.

## Supporting Information

Supporting Information is available from the Wiley Online Library or from the author.

## Acknowledgements

J.Z. and J.J. contributed equally to this work. The authors would like to acknowledge the financial support from the National "Young Thousand Talents Program," Ministry of Science and Technology of China (Grant Nos. 2014CB932200 and 2014BAI11B04) and National Natural Science Foundation of China (Grant Nos. 51573195, 21474115, and 21174147). All experimental animal procedures conducted in the present study have been approved by the Animal Care and Use Committee of General Hospital of the Chinese People's Liberation Army.

Received: October 14, 2016

Revised: January 9, 2017

Published online:

- [1] D. Taylor, J. G. Hazenberg, T. C. Lee, *Nat. Mater.* **2007**, *6*, 263.  
 [2] E. L. Fong, B. M. Watson, F. K. Kasper, A. G. Mikos, *Adv. Mater.* **2012**, *24*, 4995.  
 [3] S. J. Hollister, *Adv. Mater.* **2009**, *21*, 3330.  
 [4] T. Dvir, B. P. Timko, D. S. Kohane, R. Langer, *Nat. Nanotechnol.* **2011**, *6*, 13.  
 [5] Y. S. Pek, A. C. Wan, A. Shekaran, L. Zhuo, J. Y. Ying, *Nat. Nanotechnol.* **2008**, *3*, 671.  
 [6] L. Cao, J. Wang, J. Hou, W. Xing, C. Liu, *Biomaterials* **2014**, *35*, 684.  
 [7] P. Wang, L. Zhao, J. Liu, M. D. Weir, X. Zhou, H. H. Xu, *Bone Res.* **2014**, *2*, 14017.  
 [8] T. Troczynski, *Nat. Mater.* **2004**, *3*, 13.  
 [9] J. E. Barralet, M. Hofmann, L. M. Grover, U. Gbureck, *Adv. Mater.* **2003**, *15*, 2091.  
 [10] K. Miyazaki, T. Horibe, J. Antonucci, S. Takagi, L. Chow, *Dent. Mater.* **1993**, *9*, 41.  
 [11] Z. Sheikh, M. Geffers, T. Christel, J. E. Barralet, U. Gbureck, *Ceram. Int.* **2015**, *41*, 10010.  
 [12] M. Ginebra, M. Boltong, E. Fernandez, J. Planell, F. Driessens, *J. Mater. Sci.: Mater. Med.* **1995**, *6*, 612.  
 [13] J. Wang, M. Yang, Y. Zhu, L. Wang, A. P. Tomsia, C. Mao, *Adv. Mater.* **2014**, *26*, 4961.  
 [14] L. Zheng, F. Yang, H. Shen, X. Hu, C. Mochizuki, M. Sato, S. Wang, Y. Zhang, *Biomaterials* **2011**, *32*, 7053.  
 [15] P. Zhang, H. Wu, H. Wu, Z. Lu, C. Deng, Z. Hong, X. Jing, X. Chen, *Biomacromolecules* **2011**, *12*, 2667.  
 [16] P. Zhang, Z. Hong, T. Yu, X. Chen, X. Jing, *Biomaterials* **2009**, *30*, 58.  
 [17] C. Li, A. K. Born, T. Schweizer, M. Zenobi-Wong, M. Cerruti, R. Mezzenga, *Adv. Mater.* **2014**, *26*, 3206.  
 [18] G. Kickelbick, *Prog. Polym. Sci.* **2003**, *28*, 83.  
 [19] J. C. Reichert, A. Cipitria, D. R. Epari, S. Saifzadeh, P. Krishnakanth, A. Berner, M. A. Woodruff, H. Schell, M. Mehta, M. A. Schuetz, *Sci. Transl. Med.* **2012**, *4*, 141ra93.  
 [20] H. Fan, X. Zeng, X. Wang, R. Zhu, G. Pei, *Biomaterials* **2014**, *35*, 7407.  
 [21] V. M. Betz, O. B. Betz, T. Rosin, A. Keller, C. Thirion, M. Salomon, S. Manthey, P. Augat, V. Jansson, P. E. Müller, S. Rammelt, H. Zwipp, *J. Gene Med.* **2016**, *18*, 199.  
 [22] N. Harada, Y. Watanabe, K. Sato, S. Abe, K. Yamanaka, Y. Sakai, T. Kaneko, T. Matsushita, *Biomaterials* **2014**, *35*, 7800.  
 [23] M. J. Olszta, X. Cheng, S. S. Jee, R. Kumar, Y.-Y. Kim, M. J. Kaufman, E. P. Douglas, L. B. Gower, *Mater. Sci. Eng., R: Rep.* **2007**, *58*, 77.  
 [24] G. K. Hunter, C. L. Kyle, H. A. Goldberg, *Biochem. J.* **1994**, *300*, 723.  
 [25] A. Bigi, E. Boanini, S. Panzavolta, N. Roveri, *Biomacromolecules* **2000**, *1*, 752.  
 [26] H. Chen, M. B. Holl, B. Orr, I. Majoros, B. Clarkson, *J. Dent. Res.* **2003**, *82*, 443.  
 [27] C. Mossaad, M. Tan, M. Starr, E. A. Payzant, J. Y. Howe, R. E. Riman, *Cryst. Growth Des.* **2011**, *11*, 45.  
 [28] F. Yang, J. Wang, J. Hou, H. Guo, C. Liu, *Biomaterials* **2013**, *34*, 1514.  
 [29] S. Chen, Q. Zhang, T. Nakamoto, N. Kawazoea, G. Chen, *J. Mater. Chem. B* **2014**, *2*, 5612.  
 [30] J. Rungby, M. Kassem, E. F. Eriksen, G. Danscher, *Histochem. J.* **1993**, *25*, 446.  
 [31] W. Ge, Y. Liu, T. Chen, X. Zhang, L. Lv, C. Jin, Y. Jiang, L. Shi, Y. Zhou, *Biomaterials* **2014**, *35*, 6015.  
 [32] Y.-Y. Hu, A. Rawal, K. Schmidt-Rohr, *Proc. Natl. Acad. Sci. USA* **2010**, *107*, 22425.  
 [33] F. Yang, X. Qu, W. Cui, J. Bei, F. Yu, S. Lu, S. Wang, *Biomaterials* **2006**, *27*, 4923.